


Research Article

Stress Interferences between Fractures and Fracturing Stages of a Horizontal Well in a Sandy Conglomerate Reservoir in Junggar Basin, Northwest China

Jianmin Li,¹ Binghui Du ,² Junxiu Ma,¹ Ruining Liu,¹ Can Shi,² and Botao Lin²

¹Engineering Technology Research Institute of PetroChina Xinjiang Oilfield Branch, Karamay 834099, China

²State Key Laboratory of Petroleum Resources and Prospecting, China University of Petroleum-Beijing, Beijing 102249, China

Correspondence should be addressed to Binghui Du; binghui2358@163.com

Received 14 October 2022; Revised 13 November 2022; Accepted 31 March 2023; Published 17 April 2023

Academic Editor: Mohammed Fattah

Copyright © 2023 Jianmin Li et al. This is an open access article distributed under the Creative Commons Attribution License, which permits unrestricted use, distribution, and reproduction in any medium, provided the original work is properly cited.

The sandy conglomerate reservoirs in the Mahu oilfield located in the Junggar Basin of Northwest China are featured by a significant horizontal stress difference between two directions, making formations easy to form double-wing fractures upon hydraulic fracturing instead of creating a complex fracture network. In addition, as the well spacing or interval cluster spacing decreases, the stress interferences between hydraulic fractures strengthen accordingly, leading to more difficulties in the prediction of fracture propagation patterns. Given the geological characteristics in the study area, an extended finite element method (XFEM) based hydraulic fracture model that can handle fracturing fluid flow distribution was proposed to evaluate the seepage, stress, and damage of the formation under hydraulic fracturing. The influences of the initial stress difference, cluster spacing, and fracturing stage sequence on the hydraulic fracture stress interference and the fracture propagation were investigated, producing discoveries that include: (1) as the fractures propagate, the stress difference between two fractures changes as well, and such change is also affected by the initial stress difference and the fracture distance; (2) the postfracturing stress difference first decreases but then increases with the increase in cluster spacing; (3) as the cluster spacing increases, the interfracture stress interference decreases. In addition, the outer fractures suppress the length of the middle fractures, thus limiting the stimulated reservoir area (SRA); (4) for the cases of creating multistage fractures, the later fracturing stage experiences both the interfracture and the interstage stress interferences from the prefracturing stage. As the fracture width changes with time, the nonplanar fracture feature of the later fracturing stage becomes more evident while the corresponding SRA decreases.

1. Introduction

Unconventional oil and gas resources, such as tight oil and gas that are pervasively recognized as an essential energy supplement, are significant in ensuring the balance of supply and demand in energy structure [1]. In the past few decades, horizontal wells and multistage hydraulic fracturing have played an indispensable role in the efficient development of unconventional oil reservoirs [2, 3]. The Mahu oilfield in the Junggar Basin is a super-large tight conglomerate oilfield with reserves of 1 billion tons. In a conglomerate oil field [4, 5], the physical properties of reservoirs are poor with basically no natural fractures. Few natural fractures are obvi-

ously unfavorable for fracturing to form complex fracture network. The existing experimental and numerical results show that the formation of complex fracture network by fracturing often requires harsh conditions [6–9]. In addition, the stress difference between the two horizontal directions in Mahu oilfield is obvious, which also poses a major challenge to multistage hydraulic fracturing.

The field practice results show that severe interfracture stress interference often occurs in the process of multistage hydraulic fracturing in horizontal wells. This stress interference phenomenon exists between wells and stages and clusters [10–12], which often leads to the nonuniform expansion of multiple fractures, which in turn leads to frac hit,

seriously restricting the scale and effect of multicluster fracturing in horizontal wells. In addition, the development of fracturing technology and equipment has reduced the spacing of fracturing stages from 200 m to about 50 m [13] and the spacing of fracture clusters to 5 m [14]. The reduction of interval spacing and cluster spacing further enhances the effect of stress interference. Therefore, determining the law of fracture propagation under stress disturbance is conducive to improving the reservoir stimulation effect, which is directly related to subsequent productions.

The research on hydraulic fracture propagation mainly includes experimental research and numerical research. The physical model experiment of actual triaxial hydraulic fracturing is primarily used in experimental research. Fracturing samples are generally obtained by self-made rock samples or by collecting outcrops. Different rock properties, fracturing fluid properties, injection procedures, and three-dimensional stress states may all affect fracture initiation and propagation [15]. With the support of computed tomography (CT) and acoustic emission technology (AE) combined with tracers, the position of fracture initiation can be monitored during the experiment, and the spatial shape of the fracture can be described [16], which provides a quantitative characterization method for studying the formation law of the fracture network.

Huang and Liu [17] conducted fracturing experiments on layered samples of different lithologic rocks and studied the effects of rock physical properties and in situ stress differences. Tan et al. [18] established several fracture geometries based on substantial triaxial hydraulic fracturing experiments, providing favorable in situ stress conditions for forming complex fracture pattern networks. Kao et al. [19] used an actual triaxial hydraulic fracturing system to study the effect of different injection methods (continuous injection, variable displacement injection, and alternating injection) on fracture morphology. Although the experimental research results are true and relatively reliable, the obtained results are only at the laboratory scale. Lu et al. [20] argued that the scale effect is a main controlling factor affecting the fracture propagation process. The poor reproducibility and high cost of fracturing often lead to more realistic factors that must be considered before conducting fracturing experiments.

In terms of numerical research, the commonly used numerical simulation methods include the finite element method [21, 22], discrete element method [23, 24], boundary element method [25], and phase field method [26]. From dimensional to high-dimensional, from single-fracture to multifracture, great changes have been realized in the reformation process of fracture network construction. As a result, the hydraulic fracture propagation models have correspondingly become more and more similar to their actual counterparts. The finite element numerical simulation of multistage hydraulic fracturing in horizontal wells has always been a research hotspot. In particular, the extended finite element method (XFEM) developed based on finite element theory is favored by a large number of researchers. Compared with the traditional finite element shape function method for fracture propagation, the extended finite element method is

characterized by higher computational efficiency and accuracy. Based on the standard approximate field represented by the shape function, the method adds the extended shape function and expands the degrees of freedom. By complementing the standard degrees of freedom, researchers are able to better characterize fracture initiation, fracture effects, and the plastic strain and stress shadowing at the fracture tips [27].

Liu et al. [28] developed a fully coupled hydraulic fracture propagation model based on XFEM. The results show that the optimal cluster spacing decreases with the increase of in situ stress and is not sensitive to the change of Young's modulus of the rock matrix. Li et al. [29] proposed a fully coupled 3D model for staged fracturing in horizontal wells. In this study, the effect of perforation friction on fracture propagation was probed when multiple clusters of fractures grow. The results show that a sufficiently large perforation pressure drop can offset the stress shadow between multiple fractures and help balance the lengths of multiple fractures. Xu et al. [30] established a two-dimensional extended finite element model to study the effects of elastic modulus, Poisson's ratio, tensile strength, and minimum horizontal principal stress on the longitudinal expansion of fractures. They suggested that the interlayer-reservoir elastic modulus difference has the most significant effect on longitudinal fracture propagation.

It is worth noting that the viscous zone method (CZM) is also widely employed as the primary tool in finite element simulation. The CZM can simulate fracture propagation by presetting fracture zones, and the law of traction separation defines its constitutive model. The advantage of this approach is that stress singularities at the fracture tip in linear elastic materials can be avoided [31]. Wang et al. [32] conducted a fluid-driven fracture propagation study in the ABAQUS software and compared it with the field operation data to prove its effectiveness. Guo et al. [33] established a 2D model and successfully simulated the interaction between artificial fractures and natural weak fractures under different approach angles and geological parameters. Wang [34] performed the initial propagation of fluid-driven fractures and the interstage process between artificial and natural fractures through a zero-thickness cohesive cell (PPCZ) without presetting the propagation path. The above cases based on finite element numerical simulation mainly consider the influence of geological factors on fracture propagation but rarely involve the study of fracture propagation caused by intercluster stress interference in the lower stage of engineering parameters. Stress interference leads to the phenomenon that some well stages are not sufficiently stimulated. Therefore, it is of great significance to study the law of stress interference between fractures and stages.

The mechanism of large-scale fracturing of horizontal wells in a sandy conglomerate reservoir located in the Junggar Basin of Xinjiang province, as well as the interference between fractures and intervals, remains unclear at present. In this regard, this paper establishes a numerical model of extended finite element fracturing fractures. Based on the field data, the characterization of subcluster fractures is carried out, the dynamic process of fracturing network

formation with stress interference is analyzed, and the effect of different cluster spacing and stage spacing on fractures is quantified. The interference effect provides a theoretical basis for subsequent horizontal well fracturing in the Mahu sandy conglomerate reservoir.

2. Mathematical Framework

2.1. Rock-Fluid-Solid Coupling Process. Rock is a typical porous medium composed of rock matrix and pore structure, and rock stress is shared by rock matrix and pore fluid. According to the principle of effective stress, the equilibrium equation of the rock matrix at any time is written as [35]

$$\int_V (\bar{\sigma} - p_w I) \delta \varepsilon dV = \int_S t \cdot \delta v dS + \int_V f \cdot \delta v dV, \quad (1)$$

where σ is the effective stress matrix, Pa; p_w denotes the fluid pore pressure, Pa; $\delta \varepsilon$ is the virtual strain rate matrix, s^{-1} ; δv represents the virtual velocity vector, m/s; t is the surface force vector, N/m²; f is the physical force vector, N/m³.

The fluid flow process of fracturing conforms to the law of porous media, and the mass balance of fluid in rock can be expressed by equation (2). Assuming that the fluid flow law satisfies Darcy's law, the seepage velocity and pore pressure gradient satisfy the following equation (3):

$$\frac{1}{J} \frac{\partial}{\partial t} (J \rho_w n_w) + \frac{\partial}{\partial x} \cdot (\rho_w n_w v_w) = 0, \quad (2)$$

$$v_w = -\frac{1}{n_w g \rho_w} \cdot \left(\frac{\partial p_w}{\partial x} - \rho_w g \right), \quad (3)$$

where J is the volume change ratio of the rock, dimensionless; ρ_w stands for the fluid density, kg/m³; n_w is the porosity, dimensionless; v_w is the seepage velocity of the fluid in the solid, m/s; x is the space vector, m/s; k is the permeability matrix, m/s; g is the gravitational acceleration vector, m/s².

2.2. XFEM-Based Fracture Propagation Model. The traditional finite element method for simulating discontinuous fractures is grid-dependent, requiring the grid to satisfy geometric discontinuities and considerable mesh refinements at the fracture tip to fully capture the particular asymptotic field. At the same time, for expanding hydraulic fractures, the mesh needs to be continuously updated to match the discontinuous geometry model as the fractures change. Therefore, the traditional finite element method dramatically reduces computational efficiency. Unlike traditional finite elements, the extended finite element method introduces a locally enhanced shape function, thereby increasing the degree of freedom to ensure discontinuity. As shown in Figure 1, the above processes ensure that hydraulic fractures can initiate and propagate along arbitrary paths without remeshing.

Based on traditional finite elements, the addition of nodal enhancement functions includes a fracture tip asymptotic displacement function that captures singular points around the hydraulic fracture tip and a jump function that

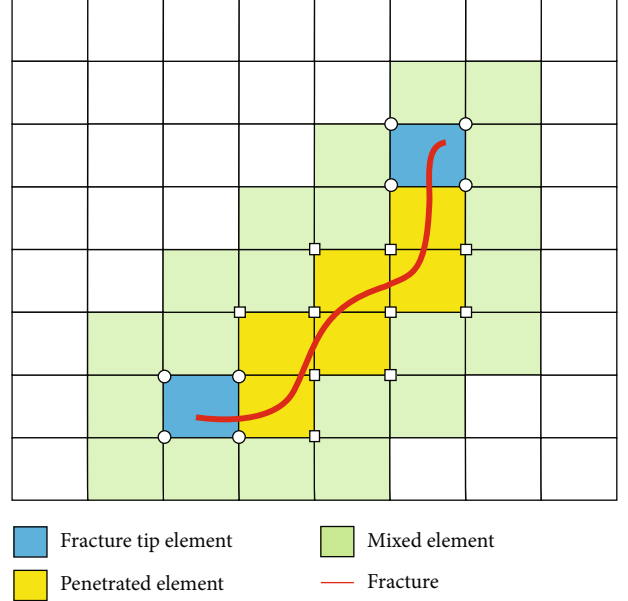


FIGURE 1: Meshes and nodes in the extended finite element method.

jumps in displacement on the fracture surface. Therefore, the displacement vector function of the fracture-enriched area can be expressed as

$$u = \sum_{I=1}^N N_I(x) \left[u_I + H(x) a_I + \sum_{\alpha=1}^4 F_{\alpha}(x) b_I^{\alpha} \right]. \quad (4)$$

In the formula, $N_I(x)$ is the conventional nodal shape function; u_I indicates the displacement vector of the continuous part; a_I is the improved degree of freedom of the node of the element penetrated by the fracture; $H(x)$ represents the jump function; b_I^{α} is the node improvement degree of freedom of the element where the crack tip is located; $F_{\alpha}(x)$ is the asymptotic displacement function of the slit tip; I is the node set of all nodes in the grid. The first term in equation (4) applies to all element nodes in the mesh, the second term applies to the nodes of the element penetrated by the fractures (see the yellow element in Figure 1), and the third term applies to the nodes of the element where the fracture tip is located (see blue cells in Figure 1).

The jump function is defined as

$$H(x) = \begin{cases} 1 & \text{if } (x - x^*) \cdot n \geq 0, \\ -1 & \text{otherwise,} \end{cases} \quad (5)$$

where x is the Gauss point of the sample; x^* is the point on the fracture near one side; n is the unit vector from the point perpendicular to the fracture outward.

The progressive displacement function of the fracture tip is defined as

$$F_\alpha(x) = \left[\sqrt{r} \sin \frac{\theta}{2}, \sqrt{r} \cos \frac{\theta}{2}, \sqrt{r} \sin \theta \sin \frac{\theta}{2}, \sqrt{r} \sin \theta \cos \frac{\theta}{2} \right], \quad (6)$$

where r is the polar axis in the slit-tip coordinate system under the polar coordinate system, m ; θ is the polar angle in the slit-tip coordinate system under the polar coordinate system, $^\circ$.

2.3. Criteria for Fracture and Damage Evolution. The damage of the fracture element obeys the traction-separation criterion, and the entire damage evolution process is divided into two stages. When the tensile stress in the fracture element does not reach the tensile strength of the reservoir rock, the corresponding displacement satisfies the linear elastic relationship [36]. When the fractured element's tensile stress reaches the rock's tensile strength, the element begins to enter the failure state [37]. After the fracture element begins to fail, the stress that the fracture can withstand gradually decreases with the increase of strain. When the upper and lower surface displacement reaches the complete failure displacement, the tensile stress on the upper and lower surfaces of the fracture element drops to zero, and the material is destroyed. The evolution process is shown in Figure 1.

This study used the maximum principal stress criterion to determine whether the damage was initiated.

$$f = \left\{ \frac{\langle \sigma_{\max} \rangle}{\sigma_{\max}^o} \right\}. \quad (7)$$

In the formula, f is the maximum principal stress ratio, dimensionless; σ_{\max} is the maximum principal stress, MPa; $\langle \rangle$ means pure compressive stress state will not cause damage; σ_{\max}^o is the allowable principal stress, MPa. When the ratio of the above two parameters f reaches 1, the fracture unit begins to be destroyed. The rock then enters a damage evolution stage where the element's stiffness gradually decreases until the material is destroyed. The corresponding expression can be expressed as

$$t = \begin{cases} (1-D)\bar{T} & \bar{T} \geq 0, \\ \bar{T} & \text{otherwise,} \end{cases} \quad (8)$$

where \bar{T} represents the three stress components calculated by the traction force separation criterion under the condition of zero damage, MPa; t is the actual stress component, MPa; D is the damage variable, $0 \sim 1$.

The BK law [38] was adopted to describe the mixed-mode damage evolution during hydraulic fracture propagation, which could be expressed as

$$G_n + (G_s - G_n) \left\{ \frac{G_s + G_t}{G_n + G_s + G_t} \right\}^\eta = G_{\text{eq}}, \quad (9)$$

TABLE 1: Parameters entered to verify model validity.

Properties	Value
Young's modulus	30 GPa
Poisson's ratio	0.35
Fluid viscosity	0.01 Pa·s
Permeability	0.5 mD
Leakoff coefficient	$6.0 \times 10^{-10} \text{ m}^3/\text{kPa} \cdot \text{s}$
Damage initiation stress	2 MPa
Critical fracture energy	30 kN/m
Specific weight of fluid	9.8 kN/m ³
Initial pore pressure	0 MPa
Maximum principle horizontal stress	47.6 MPa
Minimum principle horizontal stress	46.7 MPa
Porosity	10%
Injection rate	0.06 m ³ /s
Initial in situ stress difference	0.9 MPa
Cluster spacing	10 m

where G_n , G_s , and G_t are the critical energy release rate in three directions, respectively, N/mm; G_{eq} is the critical energy release rate of the equivalent tension-shear composite hydraulic fracture, N/mm; η is a power law coefficient ($\eta = 2$), dimensionless.

2.4. Flow Criteria in Fractured Cells. It is often used to describe the tangential flow of fracturing fluid in hydraulic fractures, including Newtonian and power-law flow. In this study, the fracturing fluid is assumed to be an incompressible Newtonian fluid, which drives fracture expansion. A portion of the fracturing fluid penetrates formations during normal flow. The lubrication equation determines the tangential flow velocity on both sides of the fracture.

$$q = -\frac{w^3}{12\mu} \nabla p. \quad (10)$$

In the formula, q is the tangential flow rate of the fracture, m³/s; w is the opening width of the fracture, m; μ is the fracturing fluid viscosity, Pa·s; ∇p is the fluid pressure gradient along the fracture direction, Pa/m.

In addition to tangential flow inside the fracture, the fracturing fluid can also be filtrated into the rock along the upper and lower surfaces of the hydraulic fractures, and the filtration behavior can be quantitatively described as

$$\begin{cases} q_t = c_t(p_i - p_t), \\ q_b = c_b(p_i - p_b), \end{cases} \quad (11)$$

where q_t and q_b are the volume flow per unit time of the upper and lower surfaces of the hydraulic fractures, respectively, m³/s; c_t and c_b are the filtration coefficients of the upper and lower surfaces of the hydraulic fractures, m³/(Pa·s); p_t and p_b are the pore pressures on the upper

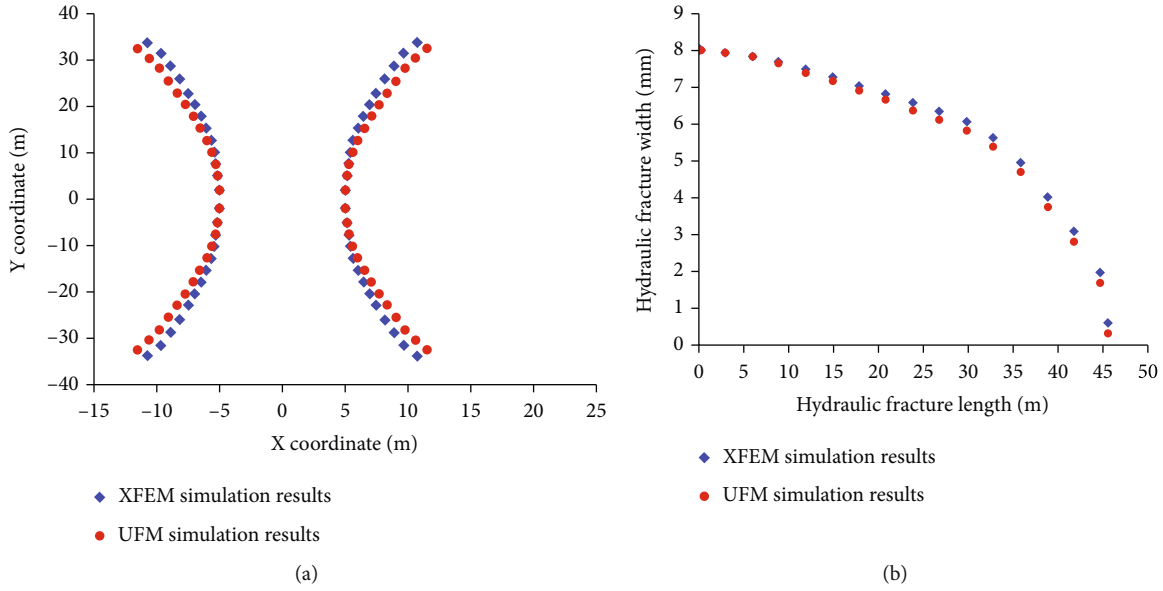


FIGURE 2: Comparison with unconventional fracture model (UFM): (a) hydraulic fracture geometry comparison and (b) comparison of hydraulic fracture length and width.

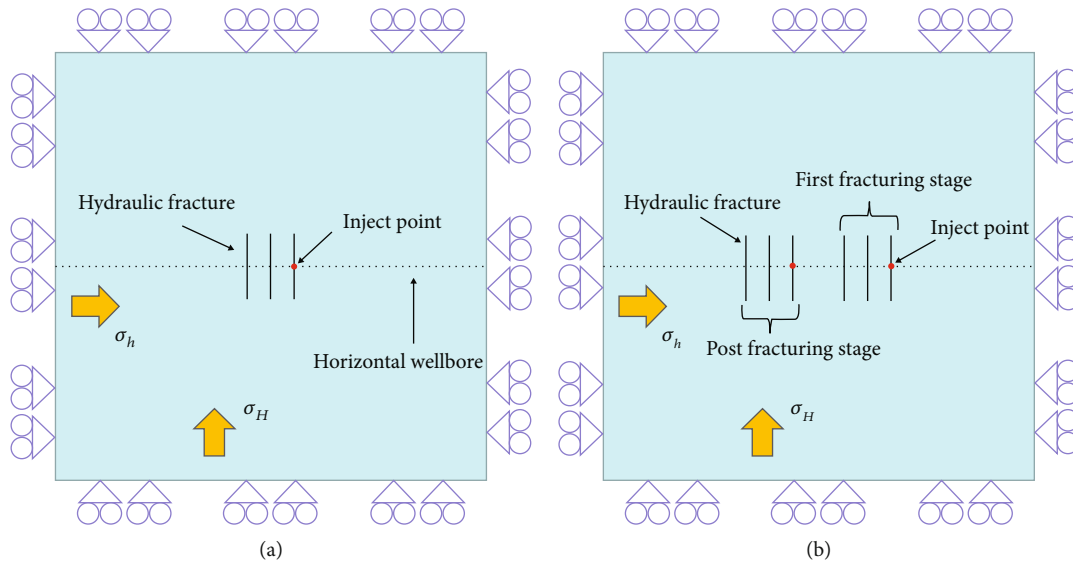


FIGURE 3: Schematic diagram of horizontal well and fracture: (a) fracturing with only one stage and (b) two-stage fracturing.

and lower surfaces of the hydraulic fractures, respectively, Pa; p_i is the fluid pressure in the hydraulic fractures, Pa.

2.5. *Pressure Loss and Flow Distribution.* Since equation (10) only characterizes the fluid flow in the fractures, the fracturing fluid filtrate is not considered. After adding the fluid loss $q_1(s)$, the mass conservation form of fracture fluid flow can be written as

$$q_1(s) = \frac{\partial w}{\partial t} + \frac{\partial q}{\partial s}, \quad (12)$$

$$\frac{\partial w}{\partial t} = \frac{\partial}{\partial s} \left(\frac{w^3}{12\mu} \frac{\partial p}{\partial s} \right) + q_1(s). \quad (13)$$

Equations (11) and (12) fully describe the continuity equation and mass conservation equation of fracturing fluid flow in fractures. The above formula takes into account the effect of fracturing fluid filtration on fracture fluid flow, which is critical for accurately characterizing fracturing fluid filtration in conglomerate reservoirs. For the fluid loss $q_1(s)$, along the fracture displacement, its specific value may change, which conforms to a function of the position [39].

During staged cluster fracturing, the fracturing fluid flows between multiple fractures and moves in the

horizontal wellbore, forming wellbore friction Δp_w , perforation friction Δp_p , and near-wellbore friction Δp_f . Considering the influence of the three frictional resistances on fluid pressure and the control of the wellbore pressure distribution and flow distribution during simultaneous multifracture propagation, the total pressure loss is

$$p_{\text{loss}} = \Delta p_w + \Delta p_p + \Delta p_f. \quad (14)$$

3. Model Building

3.1. Model Validity Verification. XFEM has been widely utilized to simulate the propagation of hydraulic fractures, and its reliability and accuracy have been verified by numerous studies [40–43]. However, some scholars proposed that the grid division method and size selection during XFEM modeling result in the difference between the results of the initial injection stage and the theoretical values. This section compares the simulation results with the unconventional fracture model developed by Weng et al. [44]. We set up two initial fractures with a cluster spacing of 10 m as the verification model. Table 1 shows the input parameters of the validation model. The numerical simulation results using this method and the simulation results of the unconventional fracture model are compared, respectively. Figure 2 shows that the two methods have a high degree of consistency in the results of fracture geometry and fracture width and length. It is proved that the simulation results of the above two models are in good agreement and are relatively reliable.

3.2. Model Building. In order to clarify the influence of stress interference caused by the competitive propagation of fractures between segments and clusters, we designed two sets of numerical models. The first set of models includes only one fracturing stage, and the second set of models includes two fracturing stages with the consideration of the fracturing sequence and interstage stress interference. In order to understand the influence of intercluster stress interference during fracturing in a specific stage of a horizontal well, we designed a two-dimensional plane strain problem with a geometric size of 800×800 m. The wellbore is symmetrically distributed in the model center (see Figure 3). A large-scale model is selected to simulate fracture propagation induced by fracture stress interference. The model uses CPE4P elements to divide the mesh and uses a refined mesh inside the model, which eliminates serious boundary effects and ensures the accuracy of the model calculation—the four boundaries of the fixed displacement. The Y and X directions represent the directions of the maximum horizontal in situ stress and the minimum horizontal in situ stress, respectively. The formation saturation and porosity are 1 and 0.1, respectively, and the initial pore pressure of the formation is 35 MPa.

During the process of simulation, the first step is to assign initial and boundary conditions to the established model. Then, the initial in situ stress field is obtained by establishing the in situ stress balance. The final step includes the fracturing fluid injection and fracture propagation. In

TABLE 2: Parameters for the hydraulic fracturing model.

Properties	Value
Young's modulus	25.4 GPa
Poisson's ratio	0.22
Fluid viscosity	0.012 Pa·s
Permeability	1.833 mD
Leakoff coefficient	$6.0 \times 10^{-10} \text{ m}^3/\text{kPa} \cdot \text{s}$
Damage initiation stress	6 MPa
Critical fracture energy	30 kN/m
Specific weight of fluid	9.8 kN/m ³
Initial pore pressure	35 MPa
Maximum principle horizontal stress	52, 56, 60, and 64 MPa
Minimum principle horizontal stress	50 MPa
Porosity	10%
Injection rate	0.0015 m ³ /s
Initial in situ stress difference	2, 6, 10, and 14 MPa
Cluster spacing	5 ~ 50 m

order to simulate the actual fracturing conditions, the model is designed with a pressure release process immediately after completing hydraulic fracturing of the first stage. Table 2 shows the rock and fracturing fluid parameters used in the model. The input of the calculation is the permeability coefficient K , which needs to be converted according to the expression $K = k\rho g/\mu$, where ρ is the fracturing fluid density, g is the gravitational acceleration, and μ is the fracturing fluid viscosity. Similarly, the conversion relationship between the void ratio and porosity directly input in the model is $e = \phi/(1 - \phi)$, where e is the void ratio, and ϕ is the porosity.

4. Simulation Result Analysis and Discussion

4.1. Influence of Stress Difference on Fracture Deflection. In the general cases of hydraulic fracturing, fractures propagate along the direction of maximum horizontal in situ stress. Even if there is a certain angle between the initial perforation orientation and the maximum horizontal in situ stress, as the fracturing continues, the subsequent fractures will gradually deflect toward the direction of the horizontal maximum in situ stress. Particularly, the greater the initial in situ stress difference, the greater the extent of fracture propagation along the maximum horizontal in situ stress. However, the above situation is only valid when a single fracture exists. When multiple fractures expand and extend simultaneously, the direction of the maximum in situ stress changes due to the stress interference generated between the fractures. As a result, some fractures deflect to a certain extent. When natural fractures exist, the deflection of the fractures may connect with more natural fractures and subsequently form a more complex fracture network.

There are many reasons for the nonplanarization of fractures due to the competitive expansion of multicluster fractures. One of the most important factors is the initial in situ stress difference. From the fracture propagation

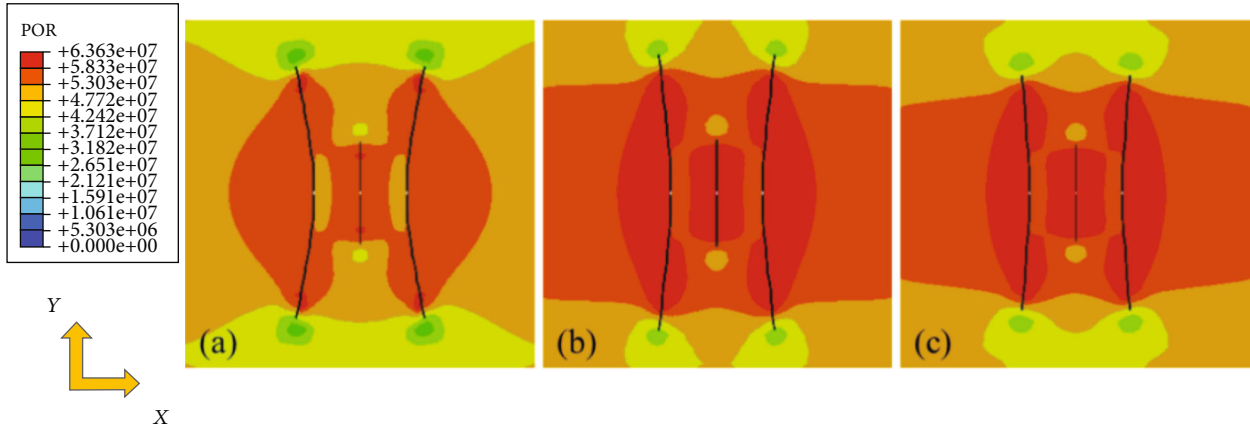


FIGURE 4: Single-stage simulation results with different initial in situ stress differences: (a) stress difference is 3 MPa; (b) stress difference is 8 MPa; (c) stress difference is 15 MPa.

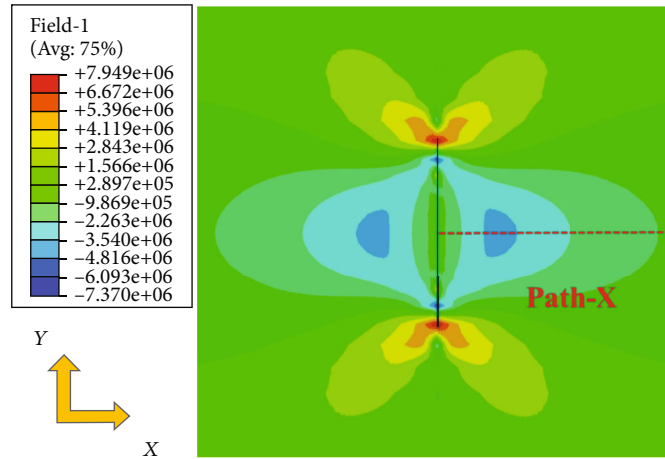


FIGURE 5: Variation results of in situ stress difference after fracturing.

situation, it can be found that the smaller the initial in situ stress difference, the greater the degree of fracture deviation from the direction of the maximum in situ stress, that is, the higher the overall degree of nonplanarization. The simulation results (see Figure 4) show that the lateral fracture deflection angles are 9°, 4°, and 2° from left to right. To a certain extent, such phenomenon indicates that the greater the in situ stress difference, the stronger the restraint force when the fractures expand, and the more simple the shape of the fracture, explaining that the high-stress difference is not conducive to the formation of complex fracture networks.

4.2. Analysis of Interfracture Stress Interference Results. Due to the crucial influence of stress difference on fracture morphology, our concern is whether the stress interference induced by multiple clusters of fracture expansion can be used to optimize the appropriate fracture spacing. Previous analyses suggest that the smaller the in situ stress difference, the higher the probability of fracture deflection and the formation of complex fractures. After simulation, it is found that another critical factor affecting fracture deflection is fracture spacing. Therefore, we set four initial in situ stress differences, which are 2 MPa, 6 MPa, 10 MPa, and 14 MPa,

respectively. On this basis, we simulated the variation of in situ stress differences when a single fracture expands.

Figure 5 shows the change result of the in situ stress difference after fracturing (i.e., the in situ stress difference after fracturing minus the initial in situ stress difference). It can be seen from Figure 5 that the stress difference near the fracture tip increases compared with the initial value, and the increase of the stress difference at the position close to the fracture tip is relatively large. However, the stress difference in the regions on both sides of the fracture surface decreases, and the decreasing trend increases and then decreases along the Path-X direction. Thus, there should be a region with the minimum stress difference when the fracturing ends. Within this range, more complex fractures can be obtained through perforating and fracturing, which provides a new insight for the rational selection of fracture spacing.

Figure 6 is obtained by outputting the cloud images under the four different initial stress differences along the Path-X direction. It can be seen from Figure 6 that the greater the initial stress difference, the more significant the reduction of the stress difference, and the closer it is to the lowest point of the stress difference. Recent studies show that when the initial stress difference exceeds 10 MPa, the maximum reduction in

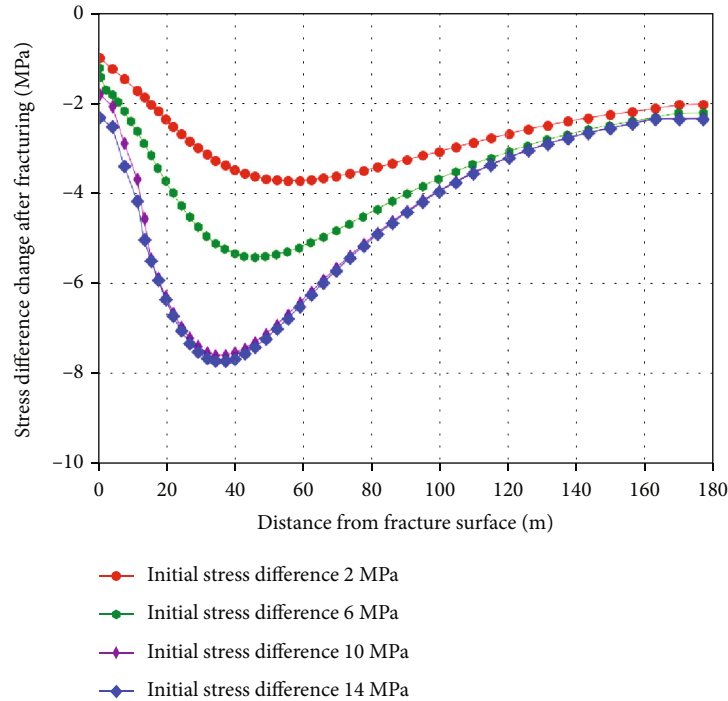


FIGURE 6: Variation results of in situ stress difference at different distances from the fracture surface.

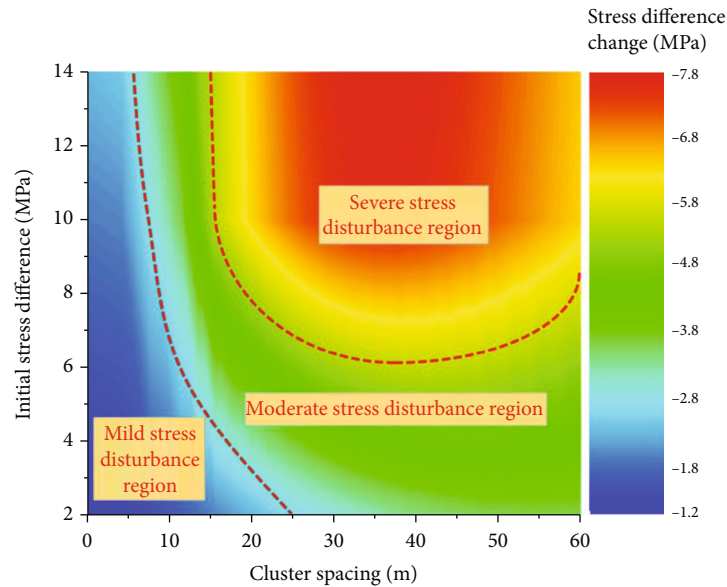


FIGURE 7: Stress disturbance limit chart used to describe variation of in situ stress difference.

the stress difference reaches about 8 MPa. It is also noted that when the initial stress difference is 2 MPa, stress reversal occurs in some areas. The smaller the initial in situ stress difference, the easier it is for the stress difference to be reversed by the stress interference associated with fracturing.

Figure 7 shows the stress interference chart with different initial in situ stress differences and cluster spacing. After fracturing, based on the change of in situ stress difference, we divided the fracturing zone into mild, moderate, and

severe interference regions. The chart shows that the stress difference decreases within 60 m from the fracture surface, but the reduction degree varies with the change of the cluster spacing and initial stress difference. When choosing a reasonable cluster spacing, we expect that the cluster spacing is within the “Severely disturbed areas,” thereby obtaining more minor in situ stress differences and increasing the complexity of the fractures. However, it can be seen from the chart that the larger the initial in situ stress difference

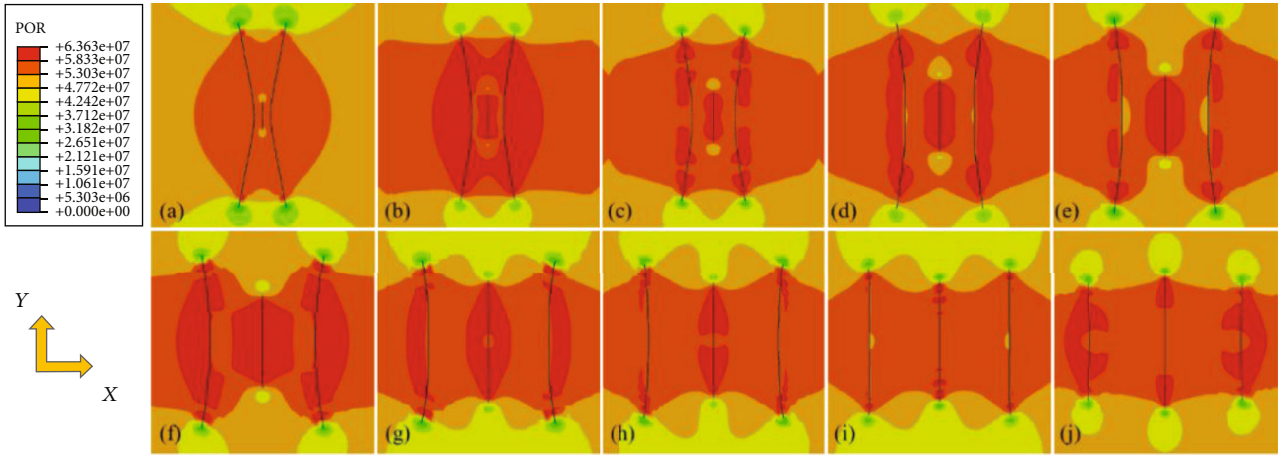


FIGURE 8: Fracture propagation at different cluster spacings: the cluster spacing of (a~j) is 5 ~ 50 m in order.

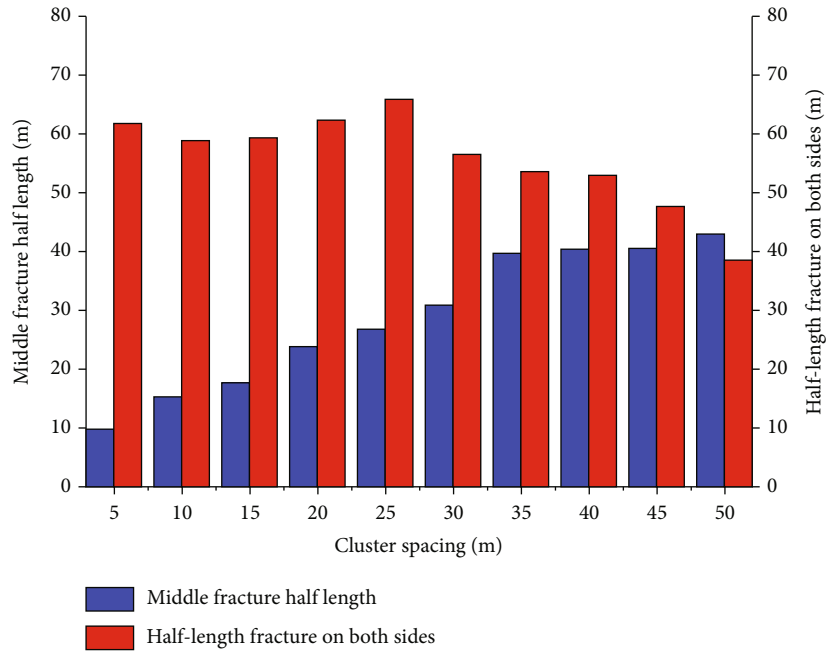


FIGURE 9: Variation of outer and middle fracture lengths with cluster spacing.

is, the smaller the optimal cluster spacing is. For example, when the initial in situ stress difference is 10 MPa, the cluster spacing should be at least 15 m or more.

The above chart can provide a reference for optimizing the appropriate fracture spacing. By searching a lower in situ stress difference area as a new perforation point, the fracturing tends to form a more complex fracture network. Based on the fracturing results, the suitable fracture spacing may vary due to overlapping of the stress difference reduction areas caused by adjacent fractures. In order to investigate the fracturing effect, except for the complexity of the fractures, one should also pay attention to the reservoir stimulation volume (SRV), which is replaced by the reservoir stimulation area (SRA). We obtained the propagation morphology of fractures under different cluster spacings by simulation.

Figure 8 shows the fracture propagation with different cluster spacings. As the cluster spacing increases, the interfracture stress interference gradually weakens, and the inhibition effect of the outer fractures on the middle fracture gradually weakens, as manifested by the continuously decreasing length of the middle fracture. When the cluster spacing is 5 m, there is a considerable difference between the middle fracture and the outer fractures. When the cluster spacing is 45 m, the lengths of the three cluster fractures are very close. When the cluster spacing is 50 m, the length of the middle fracture exceeds that of the outer fractures.

Figure 9 clearly shows the variation of fracture lengths in each cluster against cluster spacing. Similar to the stress difference change that has a region of maximum changing amount, the length of the outer fractures is also not

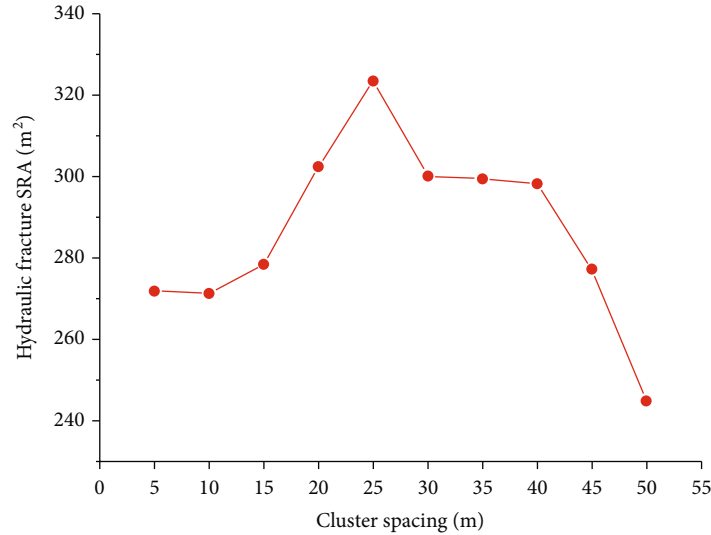


FIGURE 10: Variation of hydraulic fracture SRA with cluster spacing.

monotonously changed with the increase of cluster spacing. Instead, it experiences a process of early increase and later decrease. The variation of the intermediate fracture length is much simpler, which increases with the cluster spacing. Such phenomenon indicates that optimal cluster spacing produces the largest SRA. The calculated SRA results are shown in Figure 10. With the increase of cluster spacing, the overall SRA increased and then decreased. The maximum SRA (325.8 m^2) is obtained with a cluster spacing of 25 m, and the selected cluster spacing is set in the range of 20–30 m. Combined with the chart analysis in Figure 7, the reduction of the fracture stress difference is also remarkable within this range, and both conditions of high fracture complexity and SRA are satisfied.

Next, we simulated the effect of changing cluster number in a single stage on the overall fracturing effect. All the examples ensure that the fracturing fluid injected into each stage is the same, and the cluster spacing is selected to be 20 m. Figure 11 shows that when the injection amount of a single stage is the same, with the increase of clusters, the length of the outer fractures decreases, while the middle fracture length shows different variation laws. When the cluster number is 4 and 6, few middle fractures are able to expand effectively, resulting in a sizeable unreformed area in the middle area of the stage. When the cluster number is 5, the middle region is effectively reformed because the length of the middle fracture is close to 75 m. Figure 12 shows the SRA results in the four cases. As expected, the SRA reaches its maximum when the number of clusters is 5, peaking at 311.4 m^2 . When the cluster number is 6, the SRA is the smallest, only 280.6 m^2 , which is nearly 10% lower than that associated with the cluster number of 5.

4.3. Analysis of Interstage Fracture Stress Interference Results.

The second group of models simulates the fracturing of two adjacent fractures with the consideration of the fracturing sequence. The right stage is firstly fractured, followed by the left stage; the relevant fracturing parameters of the two

stages are the same. First, we discussed the propagation morphology of fractures in the first fracturing stage. Figure 13(a) shows the fracture morphology when the first fracturing stage is processed for 20 mins. Interfracture interference and stress shadowing inhibit the expansion of the middle fracture (HF2). In contrast, the left fracture (HF1) and the right fracture (HF3) obtain longer half-length fractures and present a certain nonplanar extended features. Figure 13(b) shows that when the first fracturing stage ends, the fracture half-lengths of the left fracture (HF1) and the right fracture (HF3) further expand from 47.0 m at 20 min to 82.6 m, while the middle fracture (the fracture half-length of HF2) only expand from 17.2 m at 20 min to 29.3 m. The growth rate of the outer fractures is significantly higher than that of the middle fracture, which indicates that the interfracture interference has a more apparent inhibitory effect on the growth of the middle fracture.

When the fractures in the second fracturing stage expand, in addition to the interfracture interference, they may also be subject to the interstage interference induced by previous fracturing stages. Figures 13(c) and 13(d) show the fracture propagation patterns at 20 min and 40 min of fracturing in the second fracturing stage, respectively. Due to the simultaneous influence of interfracture and interstage interference, the half-length of the middle fracture (HF5) in the second fracturing stage is only 23.8 m, which is 7.5 m lower than the half-length of the middle fracture (HF2) in the first fracturing stage. Meanwhile, the fracture propagation lengths on both sides of the second fracturing stage are different. The half-length of the left-hand fracture (HF4) is 78.6 m, and the half-length of the right-hand fracture (HF6) is 82.5 m, which is longer than the half-length of the left and right fractures (86.3 m) in the previous fracturing stage, respectively—lowered by 7.7 m and 3.8 m.

Compared with the simulation results in the first stage, the deflection of the fractures in the later stage is more pronounced. The nonplanar characteristics of the outer fractures are strengthened. At the same time, it is noted that

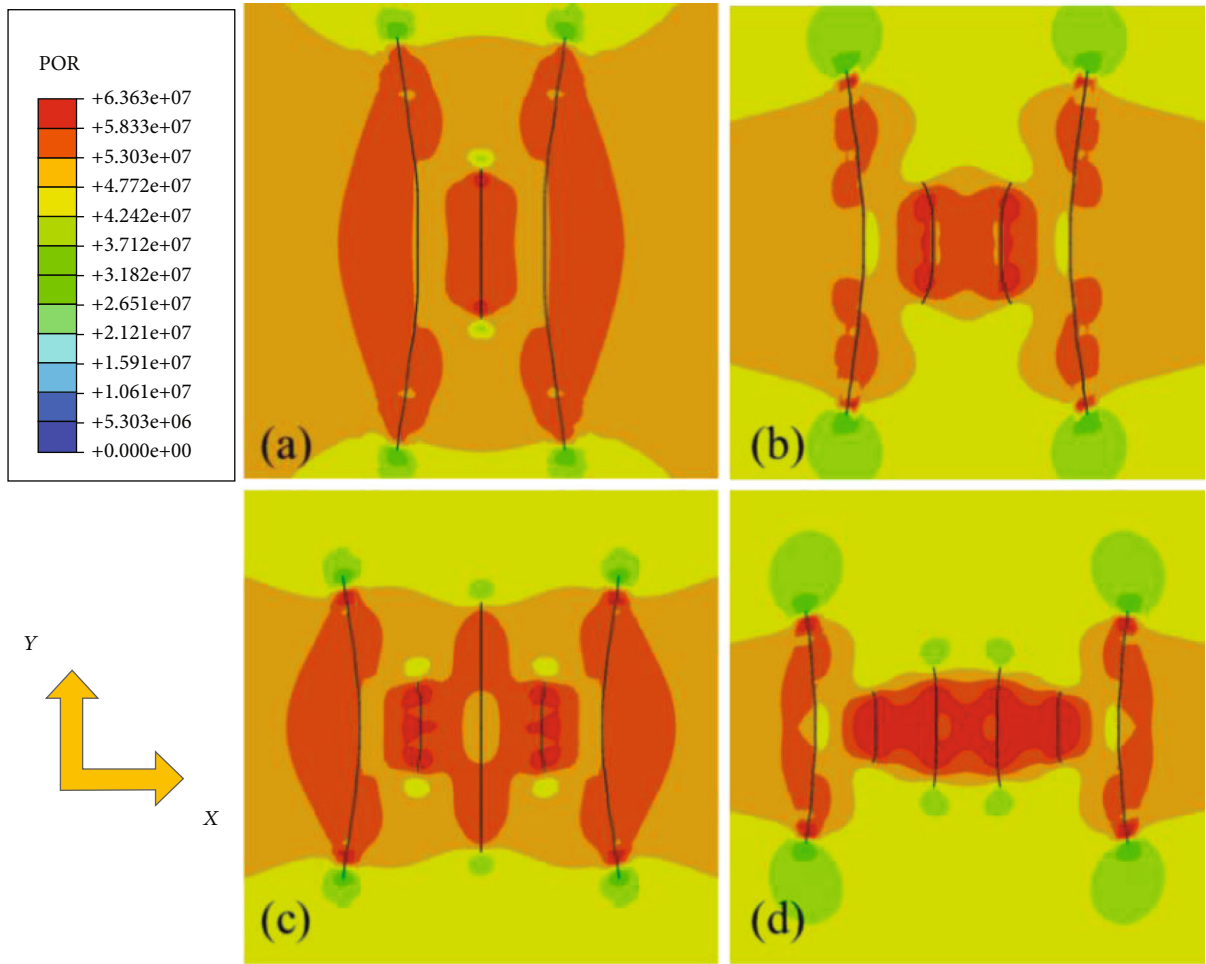


FIGURE 11: Fracture propagation results with different cluster number in a single stage.

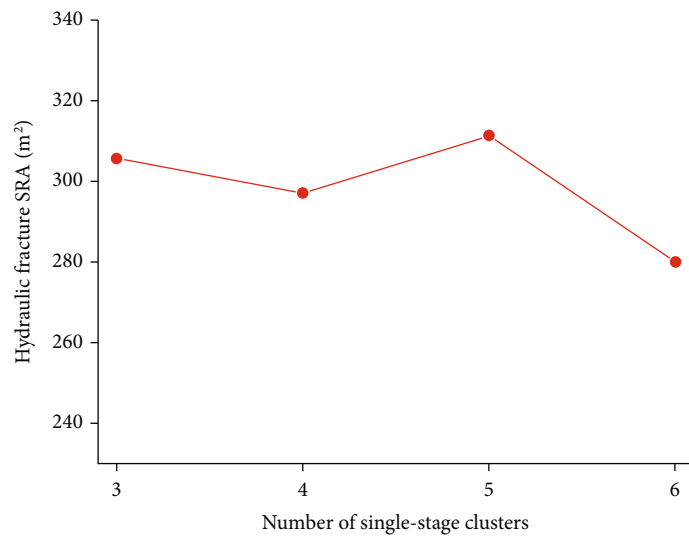


FIGURE 12: Hydraulic fracture SRA with different number of single-stage clusters.

the fractures on the left and right sides of the second fracturing stage are not entirely symmetrical. Rather, the fractures on the right side are closer to the fractures in the first frac-

turing stage and receive more substantial stress interference. Therefore, they return to the direction of the initial maximum in situ stress when deflecting to a certain extent.

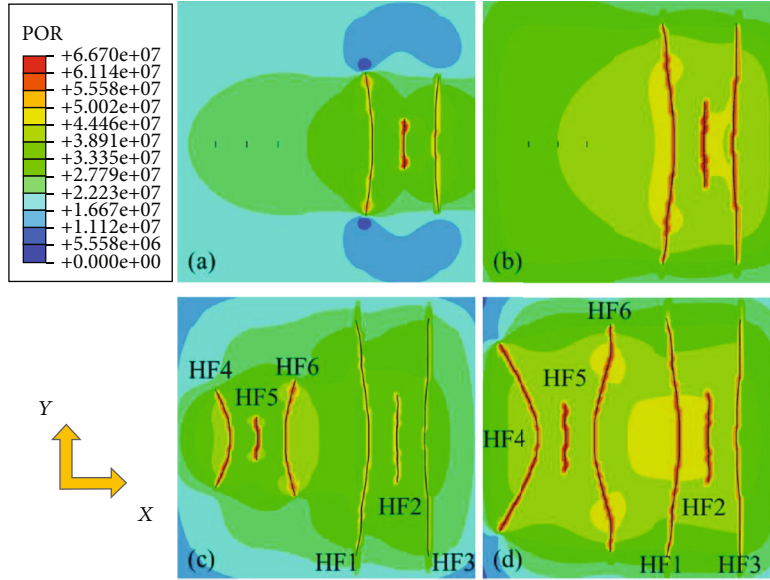


FIGURE 13: Fracturing propagation results between different stages: (a) fracturing in the first stage for 20 mins, (b) fracturing in the first stage for 40 mins, (c) fracturing in the second stage for 20 mins, and (d) fracturing in the second stage for 40 mins.

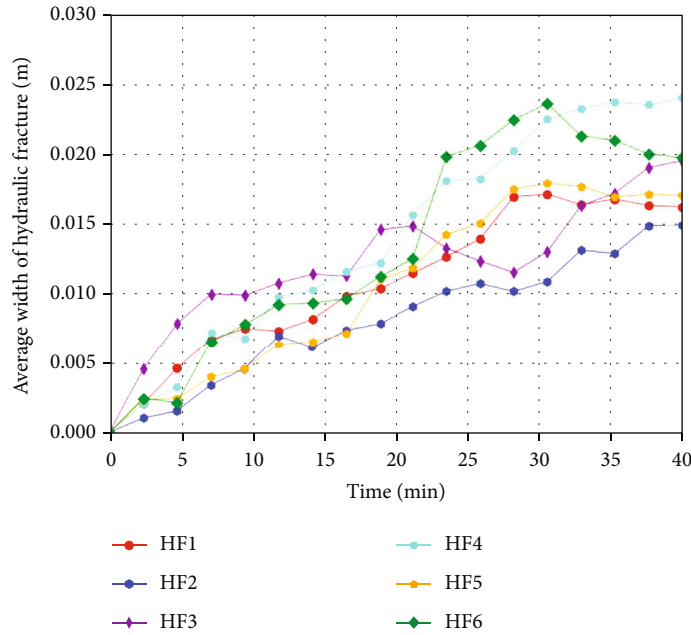


FIGURE 14: Average fracture width varies with fracturing time.

The influence of real-time interfracture interference and interstage interference on fractures is reflected in the fracture geometry change. Figure 14 shows the variation of the average fracture width of each fracture in the two fracturing stages against the fracturing time. It is prominent that the evolution characteristics of the fracture width in the two fracturing stages are complex rather than monotonic. In general, the fracture width increases as the fracturing continues, and most of the fracture widths are between 0.015 and 0.025 m. The fracture width of the first fracturing stage

is generally less than that of the latter. The fracture on the right side of the first fracturing stage (HF3) has an obvious reduction process in 20–30 min. The interfracture interference causes the reduction of the fracture width. HF3 seam length increased too fast in a short period. Since the right-side fracture (HF6) of the fracturing stage is adjacent to the first fracturing stage, the fracture width of HF6 is considerably widened and then narrowed after 20 min of fracturing, validating that HF6 is simultaneously subjected to interfracture and interstage interferences.

5. Conclusions

Aiming at the geological characteristics of large horizontal stress difference and difficult formation of complex fracture network in Junggar Basin, we established a multicluster fracture propagation model with the consideration of flow distribution. By studying the changes of different fracturing parameters on the stress difference and the degree of reservoir stimulation, we obtained the following understandings:

- (1) Fracture propagation reduces the in situ stress difference around the fracture surface. The law of in situ stress difference reduction is related to the initial in situ stress difference and cluster spacing. This law provides a new method for optimizing cluster spacing. We compared the SRA sizes obtained by the three fracture clusters with different cluster spacings. The results suggest that the horizontal well cluster spacing of 20–30 m in the Mahu sandy conglomerate reservoir in Xinjiang is the best
- (2) When the horizontal well in the Mahu reservoir is fracturing three clusters in a single stage, the interfracture interference in the same stage significantly inhibits the intermediate fractures. The fractures on both sides exhibit specific nonplanar characteristics, and as the cluster spacing increases, this inhibitory effect gradually weakens. When the cluster spacing is between 45 and 50 m, the length of the middle fractures exceeds that of the fractures on both sides, and the fracture nonplanarity characteristic is the lowest at this time. After the comparison of effects exerted by fracturing with different cluster numbers, we found that the fracture propagation is not positively correlated with the cluster number. Moreover, the fracturing effect with a cluster number of 3 and 5 in a single stage is better than that with a number of 4 and 6
- (3) For two-stage fracturing cases, the interstage and interfracture interferences are mainly reflected in the nonplanar fracture expansion process and the evolution of fracture width. Interstage interference will strengthen the nonplanar characteristics of fractures, and the fractures in the second fracturing stage will deviate from the horizontal maximum in situ stress to a greater extent. The time evolution characteristics of the fracture width of each fracture are complex. When the fractures begin to extend, their widths may remain a near constant value or may continue to widen, fluctuate, and finally narrow (such as HF6). From the perspective of SRA alone, the result of the simultaneous interfracture and interstage stress interferences is that the SRA of the second fracturing stage is smaller than that of the first stage

Overall, the analysis of stress interference between fractures and stages is a complex and comprehensive work. In actual fracturing, the stress interference between fractures

and stages occurs simultaneously. Using the law of stress interference for selecting reasonable fracturing parameters plays a positive role in obtaining satisfying fracturing effect. However, due to the fact that different geological reservoir conditions often affect the results of stress interference, the impact of interfracture and interstage stress interference on fracturing stimulation is associated with the characteristics of different cases. In addition, our future investigations will focus on the development of three-dimensional or quasi-three-dimensional fracture propagation models for better characterizing the degree of reservoir stimulation and stress interference.

Data Availability

The data used to support the findings of this study are available from the corresponding author upon request.

Conflicts of Interest

The authors declare that they have no conflicts of interest.

Acknowledgments

We sincerely appreciate the funding provided by the National Natural Science Foundation of China (no. 42277122). Gratitude is also attributed to the Xinjiang Oilfield Corporation for providing us with the field data. This work was also supported by the Xinjiang Oilfield Improvement of Shale/Tight Oil and Gas Volume Reconstruction Technology and Field Test Project.

References

- [1] C. Liu, F. Shi, D. Lu, H. Wu, H. Wang, and H. Liu, "Numerical simulation of simultaneous multiple fractures initiation in unconventional reservoirs through injection control of horizontal well," *Journal of Petroleum Science and Engineering*, vol. 159, pp. 603–613, 2017.
- [2] P. Seth, R. Manchanda, A. Kumar, and M. M. Sharma, "Analyzing pressure interference between horizontal wells during fracturing," *Journal of Petroleum Science and Engineering*, vol. 204, article 108696, 2021.
- [3] W. Cheng, G. Jiang, and Y. Jin, "Numerical simulation of fracture path and nonlinear closure for simultaneous and sequential fracturing in a horizontal well," *Computers and Geotechnics*, vol. 88, pp. 242–255, 2017.
- [4] Q. Hou, H. He, J. Li, and T. Yang, "Recent progress and prospect of oil and gas exploration by PetroChina Company Limited," *China Petroleum Exploration*, vol. 23, no. 1, pp. 1–13, 2018.
- [5] C. Jia, C. Zou, Z. Yang et al., "Significant progress of continental petroleum geological theory in basins of Central and Western China," *Petroleum Exploration and Development*, vol. 45, no. 4, pp. 573–588, 2018.
- [6] P. Tan, H. Pang, R. Zhang et al., "Experimental investigation into hydraulic fracture geometry and proppant migration characteristics for southeastern Sichuan deep shale reservoirs," *Journal of Petroleum Science and Engineering*, vol. 184, article 106517, 2020.

- [7] Z. Chen, S. Li, Z. Chen, and H. Wang, "Hydraulic fracture initiation and extending tests in deep shale gas formations and fracturing design optimization," *Petroleum Drilling Techniques*, vol. 48, no. 3, pp. 70–76, 2020.
- [8] P. Tan, Y. Jin, and G. Chen, "Differences and causes of fracture height geometry for Longmaxi shale with different burial depths in the Sichuan basin," *Petroleum Science Bulletin*, vol. 1, pp. 61–70, 2022.
- [9] L. Huang, J. Liu, F. Zhang, H. Fu, H. Zhu, and B. Damjanac, "3D lattice modeling of hydraulic fracture initiation and near-wellbore propagation for different perforation models," *Journal of Petroleum Science and Engineering*, vol. 191, article 107169, 2020.
- [10] X. Guo, K. Wu, J. Killough, and J. Tang, "Understanding the mechanism of interwell fracturing interference with reservoir/geomechanics/fracturing modeling in eagle ford shale," *SPE Reservoir Evaluation & Engineering*, vol. 22, no. 3, pp. 842–860, 2019.
- [11] X. He, J. Li, J. Wang, L. Cheng, X. Chen, and Z. Lv, "Theoretical understanding, key technologies, and field practice of high-efficiency reservoir stimulation for shale oil in Jimsar Sag," *Xinjiang Oil & Gas*, vol. 17, no. 4, pp. 28–35, 2021.
- [12] B. Kurtoglu and A. Salman, "How to utilize hydraulic fracture interference to improve unconventional development," in *Abu Dhabi International Petroleum Exhibition and Conference*, OnePetro, Abu Dhabi, UAE, 2015.
- [13] B. Maulianda, C. D. Savitri, A. Prakasan et al., "Recent comprehensive review for extended finite element method (XFEM) based on hydraulic fracturing models for unconventional hydrocarbon reservoirs," *Journal of Petroleum Exploration and Production Technology*, vol. 10, no. 8, pp. 3319–3331, 2020.
- [14] J. Zhu, J. Forrest, H. Xiong, and A. Kianinejad, "Cluster spacing and well spacing optimization using multi-well simulation for the lower Spraberry shale in Midland basin," in *SPE Liquids-Rich Basins Conference-North America*, OnePetro, Midland, Texas, USA, 2017.
- [15] B. Hou, Z. Chang, W. Fu, Y. Muhadasi, and M. Chen, "Fracture initiation and propagation in a deep shale gas reservoir subject to an alternating-fluid-injection hydraulic-fracturing treatment," *SPE Journal*, vol. 24, no. 4, pp. 1839–1855, 2019.
- [16] Y. Guo, C. Yang, and C. Jia, "Shale and fracture characterization methods research on hydraulic fracturing physical simulation," *Chinese Journal of Rock Mechanics and Engineering*, vol. 33, pp. 52–59, 2014.
- [17] B. Huang and J. Liu, "Experimental investigation of the effect of bedding planes on hydraulic fracturing under true triaxial stress," *Rock Mechanics and Rock Engineering*, vol. 50, no. 10, pp. 2627–2643, 2017.
- [18] P. Tan, Y. Jin, K. Han et al., "Analysis of hydraulic fracture initiation and vertical propagation behavior in laminated shale formation," *Fuel*, vol. 206, pp. 482–493, 2017.
- [19] J. W. Kao, Y. Jin, W. N. Fu, and Z. Chang, "Experiments research on the influence of injection method on hydraulic fracture morphology of deep shale," *Chinese Journal of Underground Space and Engineering*, vol. 15, no. 1, pp. 32–38, 2019.
- [20] Y. H. Lu, M. Chen, and S. An, "Brittle shale wellbore fracture propagation mechanism," *Petroleum Drilling Techniques*, vol. 40, no. 4, pp. 13–16, 2012.
- [21] L. Liu, L. Li, D. Elsworth, S. Zhi, and Y. Yu, "The impact of oriented perforations on fracture propagation and complexity in hydraulic fracturing," *PRO*, vol. 6, no. 11, p. 213, 2018.
- [22] Z. Chen, R. G. Jeffrey, X. Zhang, and J. Kear, "Finite-element simulation of a hydraulic fracture interacting with a natural fracture," *SPE Journal*, vol. 22, no. 1, pp. 219–234, 2017.
- [23] L. Huang, J. Liu, F. Zhang, E. Dontsov, and B. Damjanac, "Exploring the Influence of Rock Inherent Heterogeneity and Grain Size on Hydraulic Fracturing Using Discrete Element Modeling," *International Journal of Solids and Structures*, vol. 176–177, pp. 207–220, 2019.
- [24] B. Hou, Z. Chang, and E. Derek, "Simulation of competitive propagation of multi-fractures on shale oil reservoir multi-clustered fracturing in Jimsar Sag," *Acta Petrolei Sinica*, vol. 43, no. 1, pp. 75–90, 2022.
- [25] S. Cheng, M. Zhang, X. Zhang et al., "Numerical study of hydraulic fracturing near a wellbore using dual boundary element method," *International Journal of Solids and Structures*, vol. 239–240, article 111479, 2022.
- [26] M. F. Wheeler, S. Srinivasan, S. Lee, and S. Manik, "Unconventional reservoir management modeling coupling diffusive zone/phase field fracture modeling and fracture probability maps," in *SPE Reservoir Simulation Conference*, OnePetro, Galveston, Texas, USA, 2019.
- [27] T. Wang, Z. Chen, R. Wang, C. Wu, H. Xu, and Z. Hao, "A new method for cluster spacing optimization during volumetric fracturing in tight sandstone oil reservoirs," *Xinjiang Petroleum Geology*, vol. 40, no. 3, pp. 351–356, 2019.
- [28] C. Liu, X. Wang, D. Deng et al., "Optimal spacing of sequential and simultaneous fracturing in horizontal well," *Journal of Natural Gas Science and Engineering*, vol. 29, pp. 329–336, 2016.
- [29] Y. Li, J. Deng, W. Liu et al., "Numerical simulation of limited-entry multi-cluster fracturing in horizontal well," *Journal of Petroleum Science and Engineering*, vol. 152, pp. 443–455, 2017.
- [30] J. Xu, S. Han, and Z. Luo, "Analysis of factors influencing the longitudinal expansion of large sections of horizontal wells with thin interbeds," *Science Technology and Engineering*, vol. 20, pp. 2667–2673, 2020.
- [31] J. Hwang, R. Manchanda, and M. M. Sharma, "An extended finite volume model for implicit cohesive zone fracture propagation in a poroelastic medium," *Computer Methods in Applied Mechanics and Engineering*, vol. 350, pp. 571–594, 2019.
- [32] H. Wang, H. Liu, H. A. Wu, and X. X. Wang, "A 3D numerical model for studying the effect of interface shear failure on hydraulic fracture height containment," *Journal of Petroleum Science and Engineering*, vol. 133, pp. 280–284, 2015.
- [33] J. Guo, X. Zhao, H. Zhu, X. Zhang, and R. Pan, "Numerical simulation of interaction of hydraulic fracture and natural fracture based on the cohesive zone finite element method," *Journal of Natural Gas Science and Engineering*, vol. 25, pp. 180–188, 2015.
- [34] H. Wang, "Hydraulic fracture propagation in naturally fractured reservoirs: complex fracture or fracture networks," *Journal of Natural Gas Science and Engineering*, vol. 68, article 102911, 2019.
- [35] B. Xue, G. Zhang, and H. Wu, "Three-dimensional numerical simulation of hydraulic fracture in oil wells," *Journal of University of Science and Technology of China*, vol. 38, pp. 1322–1325, 2008.
- [36] M. Haddad and K. Sepehrnoori, "XFEM-based CZM for the simulation of 3D multiple-cluster hydraulic fracturing in

- quasi-brittle shale formations,” *Rock Mechanics and Rock Engineering*, vol. 49, no. 12, pp. 4731–4748, 2016.
- [37] H. Wang, “Numerical modeling of non-planar hydraulic fracture propagation in brittle and ductile rocks using XFEM with cohesive zone method,” *Journal of Petroleum Science and Engineering*, vol. 135, pp. 127–140, 2015.
- [38] M. L. Benzeggagh and M. J. C. S. Kenane, “Measurement of mixed-mode delamination fracture toughness of unidirectional glass/epoxy composites with mixed-mode bending apparatus,” *Composites Science and Technology*, vol. 56, no. 4, pp. 439–449, 1996.
- [39] W. Cheng, G. S. Jiang, and Z. D. Zhou, “Fracture competition of simultaneous propagation of multiple hydraulic fractures in a horizontal well,” *Rock and Soil Mechanics (in Chinese)*, vol. 39, pp. 4448–4456, 2018.
- [40] C. Liu, H. Liu, Y. Zhang, D. Deng, and H. Wu, “Optimal spacing of staged fracturing in horizontal shale-gas well,” *Journal of Petroleum Science and Engineering*, vol. 132, pp. 86–93, 2015.
- [41] B. Wang, F. Zhou, Y. Zou et al., “Quantitative investigation of fracture interaction by evaluating fracture curvature during temporarily plugging staged fracturing,” *Journal of Petroleum Science and Engineering*, vol. 172, pp. 559–571, 2019.
- [42] R. G. Escobar, E. C. M. Sanchez, D. Roehl, and C. Romanel, “Xfem modeling of stress shadowing in multiple hydraulic fractures in multi-layered formations,” *Journal of Natural Gas Science and Engineering*, vol. 70, article 102950, 2019.
- [43] Y. X. Chen, C. Shi, J. B. Jia, B. Lin, and Z. J. Zhang, “Interwell stress interference due to hydraulic fracturing infill well of Mahu conglomerate reservoir in Xinjiang, northwest China,” in *ARMA/DGS/SEG 2nd International Geomechanics Symposium*, OnePetro, 2021.
- [44] X. Weng, O. Kresse, C. Cohen, R. Wu, and H. Gu, “Modeling of hydraulic-fracture-network propagation in a naturally fractured formation,” *SPE Production & Operations*, vol. 26, no. 4, pp. 368–380, 2011.